

Equiareal Shape-from-Template

David Casillas-Perez · Daniel Pizarro · David Fuentes-Jimenez · Manuel Mazo · Adrien Bartoli

Received: date / Accepted: date

Abstract This paper studies the 3D reconstruction of a deformable surface from a single image and a reference surface, known as the template. This problem is known as Shape-from-Template and has been recently shown to be well-posed for isometric deformations, for which the surface bends without altering geodesics. This paper studies the case of equiareal deformations. They are elastic deformations where the local area is preserved and thus include isometry as a special case. Elastic deformations have been studied before in Shape-from-Template, yet no theoretical results were given on the existence or uniqueness of solutions. The equiareal model is much more widely applicable than isometry. This paper brings Monge’s theory, widely used for studying the solutions of non-linear first-order PDEs, to the field of 3D reconstruction. It uses this theory to establish a theoretical framework for equiareal Shape-from-Template and answers the important question of whether it is possible to reconstruct a surface exactly with a much weaker prior than isometry. We prove that equiareal Shape-from-Template has a maximum of two local solutions sufficiently near an initial curve that lies on the surface. In addition we propose an analytical reconstruction algorithm that can recover the multiple solutions. Our algorithm uses standard numerical tools for ODEs. We use the perspective camera model and

give reconstruction results with both synthetic and real examples.

1 Introduction

The reconstruction of 3D objects from images is an important goal in Computer Vision with numerous scientific and engineering applications. Over the last few decades, the reconstruction of rigid objects has been thoroughly studied and solved by Structure-from-Motion (SfM) [23], which uses multiple 2D images of the same scene. Rigidity ensures the problem’s well-posedness in the general case, which means that only one solution is obtained up to scale.

This paper studies the reconstruction of objects undergoing deformations where SfM solutions cannot be applied. This has important applications, such as augmented reality in medical endoscopy [31,22,26]. Deformable reconstruction has been actively studied over the last two decades in over a hundred articles, yet it remains an open problem in the general case. Two main scenarios have been studied: Non-Rigid Structure-from-Motion (NRSfM) [9,28,35,27,12,4,30] and Shape-from-Template (SfT) [47,8,37,12]. The former directly extends SfM to deformable objects and has attracted most of the attention from the research community. The latter recovers the object’s shape from the registration between a single image and a template, that consists of a reference shape and a texture map. Both NRSfM and SfT use constraints on the object’s deformation.

The isometric model has been thoroughly investigated for both NRSfM [24,12] and SfT [47,42,8,37,12]. Isometric deformations preserve the surface geodesics and is an accurate model for the deformation of some common materials such as paper and fabric. Recently it

David Casillas-Perez · Daniel Pizarro · David Fuentes-Jimenez · Manuel Mazo
GEINTRA, Universidad de Alcalá, Alcalá de Henares, Spain
E-mail: david.casillas@edu.uah.com;dani.pizarro@gmail.com;d.fuentes@edu.uah.es;manuel.mazo@uah.es

Adrien Bartoli · Daniel Pizarro
ISIT - CNRS/Université d’Auvergne, Clermont-Ferrand, France
E-mail: adrien.bartoli@gmail.com;dani.pizarro@gmail.com

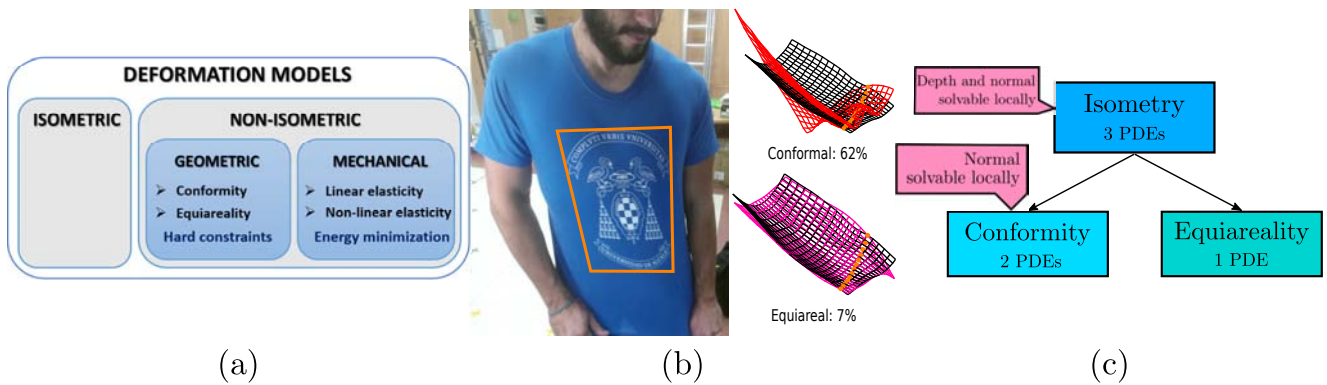


Fig. 1 Equiareality as a non-rigid deformation model. (a) Classification of non-rigid models. Equiareality belongs to the category of non-isometric geometric models. (b) Elastic stretching breaks conformity. The conformal [8] and equiareal (our method) reconstruction errors are 62% and 7%. Equiareality outperforms conformity for a wide variety of non-isometric deformations, see Fig. 11 for more examples. (c) Number of PDEs imposed by the isometric, conformal and equiareal models. Equiareality is the least constrained model, imposing only one PDE.

has been demonstrated that isometry makes SfT well-posed when the registration between the template and the input image is a known differentiable function [8]. This means that in non-degenerate cases isometric SfT has a single solution, the *true surface*, that explains the image measurements up to noise. Isometric SfT now counts with efficient methods that may obtain accurate and dense reconstruction in real-time [37].

However, isometry fails to model the deformation of extensible objects. Some recent methods have thus studied both NRSfM [6] and SfT [21, 32, 39, 33, 20] with non-isometric deformations. Two categories of models can be found, as illustrated by Fig. 1.a: mechanical and geometric models. On the one hand, the mechanical models are linear and non-linear elasticity [33, 20, 32, 21, 28]. They lead to energy-based SfT methods, whose objective is to minimize the deformation energy under boundary conditions. Because the objective is generally not in a minimal energy state, these methods do not guarantee that the true surface is reconstructed. On the other hand, the geometric models give constraints satisfied by the true surface only, similarly to the isometric model. This is a very attractive property. However, there are very few geometric models. One of them is the angle-preserving conformity [8], which is however rarely applicable in practice, as can be seen in Fig. 1.b. Mechanical SfT methods model elasticity well but do not handle the possible existence of multiple solutions. Geometric SfT methods compute all possible multiple solutions as and when they occur.

We study SfT for equiareal deformations, which is a geometric non-isometric model. Fig. 1.c shows the hierarchy between the isometric, conformal and equiareal models. Equiareal and conformal deformations are fundamentally different as none imply the other. However, both are implied by isometry and together they im-

ply isometry, showing their high-level of complementarity. Equiareal SfT can be described with a single Partial Differential Equation (PDE) and is thus weaker than conformal SfT, which results in a system of two PDEs. We can thus see the equiareal deformation as a ‘limit’ geometric model. It is also much more applicable than the conformal model. Our real data experiments show that equiareal SfT is accurate for common non-isometric objects such as clothes and outperforms the isometric and all the evaluated non-isometric SfT methods.

We provide a complete framework for solving equiareal SfT by expressing the problem as a quadratic first-order PDE in two variables, the spatial coordinates of the input image. We include a study of the problem’s well-posedness, a characterization of the boundary conditions and of the possible ambiguities, and a fast analytical reconstruction algorithm based on standard ODE solvers. By analytical algorithm, we mean an algorithm whose convergence in a finite number of steps is guaranteed, and which returns the problem’s multiple solution, if any. We base our framework on Monge’s theory, which is widely used to study the solutions of first-order non-linear PDEs, but was never used to study deformable reconstruction. Monge’s theory allows us to establish the following two preliminary results: 1) given a point belonging to the initial strip¹ it establishes the conditions of existence and uniqueness of solutions of the PDE in a local domain of the point and 2) for each point of the initial strip where the previous conditions are met, there exists a system of ODEs, called the characteristic system, whose unique solution is a strip that belongs to the solution of the PDE.

¹ A strip is a curve and its normal field on the surface.

We use the two preliminar results to form our four core contributions. *i)* We answer the question of whether one can reconstruct the surface exactly with a much weaker prior than isometry: we show that equiareal SfT simply requires an initial curve that belongs to the true surface to bound the amount of solutions. *ii)* We study the conditions to guarantee solution uniqueness in equiareal SfT, given an initial curve. We extend Monge’s local uniqueness condition by finding its spatial limits, partitioning the image domain in regions where solution uniqueness is guaranteed. We show that crossing these limits generates multiple solutions in general. We establish an upper bound on the number of global solutions and study the impact of the initial curve on solution uniqueness. *iii)* We propose a reconstruction method based on sampling the initial curve and solving the characteristic system using standard ODE numerical solvers. This allows us to reconstruct the surface (and all the additional solutions) by using convex numerical integration of a discrete number of characteristic strips. *iv)* We show that equiareal SfT is promising to reconstruct a wide variety of real objects, both isometric and non-isometric, with high accuracy, outperforming the existing isometric and non-isometric SfT methods which we compared with.

2 Previous Work

Deformable 3D reconstruction was first proposed for solving NRSfM by modelling deformations using a linear shape basis [9]. This statistical model works well for objects with simple deformations. The method is based on low-rank factorization and suffers from ambiguities. Many works that followed [9] improved well-posedness by including shape [13] or smoothness [27,38] constraints. Other methods such as the shape-trajectory basis [7,19] extended the shape basis formulation [9]. Recently [52] showed that direct trace minimization of the measurement matrix reduces the amount of ambiguities and resolved the need for a fixed amount of shape vectors. Based on this approach, [17] proposed one of the first dense NRSfM approaches for video sequences. Physics-based modelling for NRSfM is more recent. It handles more complex deformations and works with fewer images as compared to statistics-based modelling. Most of these methods, for instance [44,40,24,1,45], use isometry as a deformation model, except [3,6,5,4] which model deformations with elasticity. In addition, some works include other cues such as shading and motion [30,50] or silhouettes [35]. Despite the amount of existing methods, the accuracy and the stability of NRSfM methods is still far from the results of SfM.

The SfT methods, also called template-based, [47,42,8,37,12,10,46,48,51] assume a previous 3D model known as the template of the object. They are mostly based on physics-based deformation models. SfT is better constrained than NRSfM and is suitable for many applications where the template is known or can be acquired using SfM.

We group existing SfT methods by the type of deformation constraint they impose on the object’s surface. The most popular model is isometry, which makes SfT a well-posed problem, as showed in [8]. We thus distinguish between isometric and non-isometric methods. In isometric SfT, we find differences in the way the existing methods impose the isometry constraints: *i)* zeroth-order methods based on inextensibility [48,46,47,42,51,37], *ii)* analytical solutions from quadratic PDEs [8,12] and *iii)* iterative refinement methods [10,39]. Methods in *i)* are based on convex optimization. They relax isometry with inextensibility and the so-called maximum depth heuristic [42,47]. Methods in *ii)* model isometric SfT with a system of quadratic PDEs. They propose analytical solutions for depth and depth gradient by finding the non-holonomic solutions of the PDE. Refinement methods in *iii)* require non-convex optimization and are very accurate, given a good initialization provided by a method from *i)* or *ii)*. Recently [37] showed real-time implementations of isometric SfT that obtain accurate and dense reconstructions in videos. Additionally, some SfT works include shading and motion cues [36], combine shading with contours [16] or include the silhouette [10] to improve SfT solutions for poorly textured objects.

Non-isometric models have been proposed such as conformity [8], that preserves angles, linear elasticity [2,32,39] and non-linear elasticity [33,20,21]. In conformal SfT [8], the problem admits a finite number of solutions, obtained from analytical non-holonomic solutions of the depth gradient. All existing methods based on linear and non-linear elasticity optimize a variational cost based on either FEM models [32,21,4,33,20] or particle systems [39]. These methods require boundary conditions. The type and amount of boundary conditions has a significant effect on the solution but this has only been observed empirically. This makes non-isometric SfT an open problem.

Our equiareal model is accurate to model a wide range of elastic deformations. As isometric and conformal SfT, equiareal SfT is required one to solve a quadratic first-order PDE. We show that the problem requires boundary conditions to be well-posed and we give a theoretical bound to the number of solutions given the boundary conditions. We also propose a very efficient and fast reconstruction algorithm based on

ODE solvers. As shown in Sect. 5, our method outperforms the elastic SfT methods we compared with in terms of speed and accuracy.

3 Problem Formulation

3.1 Notation

Italic upper-case characters denote both regular surfaces embedded in \mathbb{R}^3 , such as \mathcal{T} , and open subsets of the usual topology of \mathbb{R}^2 used in surface parametrizations. A surface parametrization is represented by a pair (\mathcal{U}, X_t) , where \mathcal{U} is the domain set of the function, frequently the image, and $X_t : \mathcal{U} \rightarrow \mathbb{R}^3$ is a parametrization function, represented by an upper-case letter with a single subscript. Greek upper-case characters are used for maps between surfaces, *e.g.* the equiareal map Ψ , and greek lower-case characters denote maps between subsets of \mathbb{R}^2 , *e.g.* the warp η . The composition of mappings is represented by the \circ operator. Strips are oriented 5-dimensional curves as we will describe precisely in Sect. 4.2. We use t to parametrize the characteristic strips and s to parametrize the initial strips as explained in Sect. 4.2. The symbol $\|\cdot\|$ refers to the Euclidean norm. We consider row vectors of the Euclidean vector space \mathbb{R}^3 and we represent them as (x, y, z) . Points in the image are represented by the row coordinate vectors (u, v) . We use the canonical basis in both cases.

3.2 Geometric Modeling

3.2.1 General Points

Fig. 2 illustrates the geometric modeling of the problem. Let $\mathcal{T} \subset \mathbb{R}^3$ be a known regular parametric surface and let (\mathcal{U}, X_t) be one of its parametrizations. The surface \mathcal{T} is the template. Let $\mathcal{S} \subset \mathbb{R}^3$ be the regular parametric surface that results from an equiareal transformation $\Psi \in \mathcal{C}^2(\mathcal{T}, \mathbb{R}^3)$ of the template \mathcal{T} . We define equiareal maps and their properties rigorously in Sect. 3.3. The equiareal map Ψ is a diffeomorphism between the template \mathcal{T} and the deformed surface \mathcal{S} . It thus preserves the topology of \mathcal{T} and avoids self-intersections. Both \mathcal{S} and Ψ are unknown.

A camera projects \mathcal{S} in the image plane, represented by the open subset $\mathcal{I} \subset \mathbb{R}^2$. We assume the surface is never self-occluded in the image and thus each point in \mathcal{S} is uniquely projected into \mathcal{I} . Therefore, there exists a unique parametrization of \mathcal{S} from the image plane, namely (\mathcal{I}, X_i) , where $X_i \in \mathcal{C}^2(\mathcal{I}, \mathbb{R}^3)$ denotes

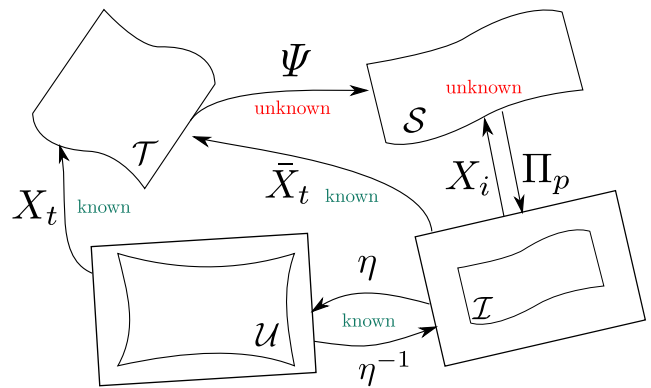


Fig. 2 The diagram shows the differential geometric model we use to study equiareal SfT. The known template \mathcal{T} is transformed by an equiareal map into the unknown surface \mathcal{S} which is projected with a perspective camera Π_p to create the image \mathcal{I} . Assuming the warp η is known, our objective is to recover the unknown surface \mathcal{S} through one of its parametrizations (\mathcal{I}, X_i) . In this diagram one can find identities by following different paths that connect the domains. The arrows represent functions and we can thus follow them by function composition (for instance we have $\bar{X}_t = X_t \circ \eta$). See Sect. 3.2.1 for details.

the image embedding of \mathcal{S} . We use the perspective camera model with known intrinsic parameters. The warp function and its inverse are known and represented by $\eta \in \mathcal{C}^2(\mathcal{I}, \mathbb{R}^2)$ and $\eta^{-1} \in \mathcal{C}^2(\mathcal{U}, \mathbb{R}^2)$ respectively. Both of them are two-diffeomorphisms, that is, twice continuously differentiable bijective maps between the image $\mathcal{I} \subset \mathbb{R}^2$ and the parametrization space $\mathcal{U} \subset \mathbb{R}^2$ of the template.

According to the commutative graph in Fig. 2 we can parametrize the template \mathcal{T} from the image \mathcal{I} , which we denote by (\mathcal{I}, \bar{X}_t) , where $\bar{X}_t = X_t \circ \eta$. As both η and X_t are known, \bar{X}_t is available.

3.2.2 Camera Model and Image Embedding

We assume that the image plane is at $z = 1$ in camera coordinates, which is achieved by working in retinal coordinates. The perspective projection of a point (x, y, z) is then given by:

$$\begin{aligned} \Pi_p : \quad \mathbb{R}^3 &\mapsto \mathbb{R}^2 \\ (x, y, z) &\mapsto \begin{pmatrix} x & y \\ z & z \end{pmatrix}, \end{aligned} \quad (1)$$

where the restriction $\Pi_p|_{\mathcal{S}} : \mathcal{S} \mapsto \mathbb{R}^2$ of Π_p to the surface \mathcal{S} is bijective. The inverse of this restriction is the *image embedding*. It consists of a depth based parametrization of the surface (\mathcal{I}, X_i) expressed in terms of the depth function $\rho : \mathbb{R}^2 \mapsto \mathbb{R}$:

$$X_i(u, v) = \rho(u, v) (u, v, 1). \quad (2)$$

Alternatively to ρ , we define the Euclidean distance between the camera's projection origin and the surface point as $\tilde{\rho} : \mathbb{R}^2 \mapsto \mathbb{R}$:

$$\tilde{\rho}(u, v) = \rho(u, v)\varepsilon, \quad (3)$$

where $\varepsilon = \sqrt{1 + u^2 + v^2}$. Now, the perspective parametrization (\mathcal{I}, X_i) can be expressed in terms of $\tilde{\rho}$ as:

$$X_i(u, v) = \frac{\tilde{\rho}(u, v)}{\varepsilon} (u, v, 1). \quad (4)$$

As will be shown, working with $\tilde{\rho}$ instead of ρ greatly simplifies the reconstruction equations.

3.3 Equiareal Maps

Let $\Psi : S_1 \mapsto S_2$ be a diffeomorphism between two surfaces. Ψ is an equiareal map if the area of each open set $U \subset S_1$ is equal to the area of its image $\Psi(U) \subset S_2$. Alternatively, using the pushforward function, it is common to define equiareal maps as follows.

Definition 1 A diffeomorphism $\Psi : S_1 \mapsto S_2$ between surfaces in \mathbb{R}^3 is an equiareal map if for each point $\mathbf{p} \in S_1$, the pushforward function $d\Psi_{\mathbf{p}} : T_{\mathbf{p}}S_1 \mapsto T_{\Psi(\mathbf{p})}S_2$ of Ψ in \mathbf{p} obeys:

$$\|\mathbf{w} \times \mathbf{h}\| = \|d\Psi_{\mathbf{p}}(\mathbf{w}) \times d\Psi_{\mathbf{p}}(\mathbf{h})\| \quad (5)$$

where $\mathbf{w}, \mathbf{h} \in T_{\mathbf{p}}S_1$ are any two vectors of the tangent plane of S_1 at \mathbf{p} .

We recall that $\|\mathbf{w} \times \mathbf{h}\|$ is the area of the parallelogram defined by the vectors \mathbf{w} and \mathbf{h} . Isometric maps preserve distances, angles and areas and thus every isometric map is equiareal. Equiareal maps can also be characterized in differential geometry as maps that preserve the determinant of the first fundamental form.

Theorem 1 A diffeomorphism $\Psi : S_1 \mapsto S_2$ between surfaces in \mathbb{R}^3 is an equiareal map if and only if it preserves the determinant of the first fundamental form.

Proof Let (\mathcal{U}, X) be a parametrization of S_1 and let $\{X_u, X_v\}$ be a basis of the tangent plane $T_{\mathbf{p}}S_1$ of S_1 in \mathbf{p} . Using Lagrange's identity we have:

$$\|X_u \times X_v\|^2 + \langle X_u, X_v \rangle^2 = \|X_u\|^2 \|X_v\|^2. \quad (6)$$

Remembering that $E = \langle X_u, X_u \rangle$, $F = \langle X_u, X_v \rangle$, $G = \langle X_v, X_v \rangle$, then:

$$\begin{aligned} \|X_u \times X_v\|^2 &= \|X_u\|^2 \|X_v\|^2 - \langle X_u, X_v \rangle^2 \\ &= EG - F^2 = \left| \begin{pmatrix} E & F \\ F & G \end{pmatrix} \right|. \end{aligned} \quad (7)$$

As from Definition 1 equiareal maps preserve the modulus of the cross product between any two different vectors of the tangent plane, they must thus preserve the determinant of the first fundamental form, and vice versa. \square

4 Equiareal Shape-from-Template

4.1 Establishing the Reconstruction PDE

We describe equiareal SfT as a first-order PDE in the depth function $\tilde{\rho}$ defined in equation (4). We denote by $U_i(u, v) = EG - F^2$ and $\bar{U}(u, v) = \bar{E}\bar{G} - \bar{F}^2$ the determinant of the first fundamental form of X_i and \bar{X}_t respectively at point $(u, v) \in \mathcal{I}$. From the commutative diagram of Fig. 2 we have that $X_i = \Psi \circ \bar{X}_t$ with Ψ an equiareal map. From Theorem 1 we find the following identity:

$$U_i(u, v) = \bar{U}(u, v), \quad (8)$$

where we recall that \bar{U} is a known function obtained from X_t , η and their first derivatives.

Using equation (4), the coefficients of the first fundamental form of \mathcal{S} are derived as follows:

$$\begin{aligned} E &= \langle X_{iu}, X_{iu} \rangle = \tilde{\rho}_u^2 + \frac{\tilde{\rho}^2(1+v^2)}{(1+u^2+v^2)^2} = \tilde{\rho}_u^2 + \frac{\tilde{\rho}^2(1+v^2)}{\varepsilon^4} \\ F &= \langle X_{iu}, X_{iv} \rangle = \tilde{\rho}_u \tilde{\rho}_v - \frac{\tilde{\rho}^2 uv}{(1+u^2+v^2)^2} = \tilde{\rho}_u \tilde{\rho}_v - \frac{\tilde{\rho}^2 uv}{\varepsilon^4} \\ G &= \langle X_{iv}, X_{iv} \rangle = \tilde{\rho}_v^2 + \frac{\tilde{\rho}^2(1+u^2)}{(1+u^2+v^2)^2} = \tilde{\rho}_v^2 + \frac{\tilde{\rho}^2(1+u^2)}{\varepsilon^4} \end{aligned} \quad (9)$$

where $X_{iu} = \frac{\partial X_i}{\partial u}$, $X_{iv} = \frac{\partial X_i}{\partial v}$, $\tilde{\rho}_u = \frac{\partial \tilde{\rho}}{\partial u}$ and $\tilde{\rho}_v = \frac{\partial \tilde{\rho}}{\partial v}$. The determinant of the first fundamental form of \mathcal{S} is then:

$$\begin{aligned} U_i(u, v) &= EG - F^2 = \\ &= \frac{\tilde{\rho}^4}{\varepsilon^6} + \frac{\tilde{\rho}^2}{\varepsilon^4} (\tilde{\rho}_u^2(1+u^2) + \tilde{\rho}_v^2(1+v^2) + 2\tilde{\rho}_u \tilde{\rho}_v uv). \end{aligned} \quad (10)$$

We now apply the following change of variable to equation (10):

$$\tilde{x} = \tilde{\rho}^2 \quad (11)$$

which implies $\tilde{x}_u = \frac{\partial \tilde{x}}{\partial u} = 2\tilde{\rho} \tilde{\rho}_u$ and $\tilde{x}_v = \frac{\partial \tilde{x}}{\partial v} = 2\tilde{\rho} \tilde{\rho}_v$. We then obtain the following quadratic first-order PDE, which we call the *reconstruction PDE*:

$$\begin{aligned} \frac{\tilde{x}^2}{\varepsilon^6} + \frac{1}{\varepsilon^4} \left(\frac{\tilde{x}_u^2}{4}(1+u^2) + \frac{\tilde{x}_v^2}{4}(1+v^2) + \frac{\tilde{x}_u \tilde{x}_v}{2} uv \right) \\ = \bar{U}(u, v). \end{aligned} \quad (12)$$

Equation (12) is a non-autonomous quadratic PDE that depends on the squared depth function \tilde{x} , its partial derivatives \tilde{x}_u and \tilde{x}_v , the image coordinates u, v and \bar{U} . Let \tilde{x}^* be a solution of equation (12). Assuming that \tilde{x}^* does not change the sign in its domain \mathcal{I} then we have:

$$X_i(u, v) = \frac{\sqrt{|\tilde{x}^*(u, v)|}}{\varepsilon} (u, v, 1). \quad (13)$$

Without additional constraints, such as initial or boundary conditions, the PDE (12) is ill-posed and in the general case does not have an analytic solution. We propose to solve it with numerical methods and to study the influence of the initial conditions on the existence and uniqueness of solutions.

4.2 Monge's Theory and the Characteristic Method

We give a simple introduction to *Monge's theory* and *the characteristic method* to find and study the solutions of the reconstruction PDE. This theory copes with general first-order non-linear PDEs and we refer the reader to [14,25] for details and rigorous proofs and to [34] for the original manuscripts and theory developed by Gaspard Monge.

Given a general non-linear PDE in two variables:

$$F(u, v, x, p, q) = 0, \quad (14)$$

where $F \in \mathcal{C}^2(\Omega)$ and $\Omega \subset \mathbb{R}^5$ is an open domain, u, v are the independent variables, x is the unknown function and $p = x_u, q = x_v$ its derivatives. A solution of equation (14) can be seen as the surface $(u, v, x(u, v))$, usually known as the *solution surface* \mathcal{S}_s .

We define a strip as a general curve in 5 dimensions $r(t) : I \subset \mathbb{R} \rightarrow \mathbb{R}^5$ with $r(t) = (u(t), v(t), x(t), p(t), q(t))$. The 5-dimensional strip has a geometric interpretation in \mathbb{R}^3 . The first three components form a spatial curve $\gamma(t) : I \subset \mathbb{R} \rightarrow \mathbb{R}^3$ and the two last components $(p(t), q(t))$ give the normal vector of \mathcal{S}_s along the curve $\gamma(t)$ as:

$$(-p(t), -q(t), 1). \quad (15)$$

In Monge's theory, given the PDE (14), one defines the following system of five first-order ODEs:

$$\begin{cases} \frac{du}{dt} = F_p \\ \frac{dv}{dt} = F_q \\ \frac{dx}{dt} = pF_p + qF_q \\ \frac{dp}{dt} = -F_u - pF_x \\ \frac{dq}{dt} = -F_v - qF_x, \end{cases} \quad (16)$$

where F_u, F_v, F_x, F_p, F_q are the partial derivatives of F with respect to the coordinates in Ω . The ODE system (16) is called the *characteristic system* and its solutions are called the *characteristic strips*. Each characteristic strip $r(t)$ contains a three dimensional curve $\gamma(t)$ called the *characteristic curve*, see Fig. 3. The characteristic system is a central result in Monge's theory and has a non-trivial derivation [25].

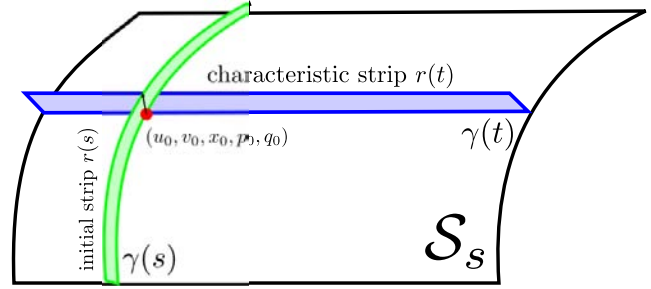


Fig. 3 We represent the initial strip $r(s)$ with its initial curve $\gamma(s)$ (green) and the characteristic strip $r(t)$ with its characteristic curve $\gamma(t)$ (blue) computed from a point $(u_0, v_0, x_0, p_0, q_0)$ of $r(s)$.

The main property of a characteristic strip $r(t)$ is that it gives $f(t) = F(r(t)) = F(u(t), v(t), x(t), p(t), q(t))$ a constant value. This is established by simply differentiating $f(t)$ and substituting the equations of the characteristic system (16):

$$\begin{aligned} \frac{df}{dt} &= F_u \frac{du}{dt} + F_v \frac{dv}{dt} + F_x \frac{dx}{dt} + F_p \frac{dp}{dt} + F_q \frac{dq}{dt} = \\ &= F_u F_p + F_v F_q + F_x (pF_p + qF_q) + \\ &+ F_p (-F_u - pF_x) + F_q (-F_v - qF_x) = 0. \end{aligned} \quad (17)$$

Consequently, a characteristic strip calculated for any point $(u_0, v_0, x_0, p_0, q_0) \in \Omega$ that satisfies the PDE (14) also satisfies the PDE. This property forms the heart of our reconstruction algorithm.

Equation (18) shows the characteristic system associated with the reconstruction PDE (12):

$$\begin{cases} \frac{du}{dt} = \frac{p(u^2 + 1) + qv}{2\varepsilon^4} \\ \frac{dv}{dt} = \frac{q(v^2 + 1) + pu}{2\varepsilon^4} \\ \frac{dx}{dt} = \frac{p^2 u^2 + p^2 + 2pqv + q^2 v^2 + q^2}{2\varepsilon^4} \\ \frac{dp}{dt} = \bar{U}_u + \frac{6u\tilde{x}^2}{\varepsilon^8} - \frac{2\varepsilon^4 (up^2 + qvp)}{\varepsilon^6} \\ \quad + \frac{u(p^2(u^2 + 1) + q^2(v^2 + 1) + 2pqv) - 2p\tilde{x}}{\varepsilon^6} \\ \frac{dq}{dt} = \bar{U}_v + \frac{6v\tilde{x}^2}{\varepsilon^8} - \frac{(vq^2 + puq)}{2\varepsilon^4} \\ \quad + \frac{v(p^2(u^2 + 1) + q^2(v^2 + 1) + 2pqv) - 2q\tilde{x}}{\varepsilon^6} \end{cases}$$

(18)

We observe that one can compute *characteristic strips* by solving the *characteristic system* (18) from points in the surface (u_i, v_i, \tilde{x}_i) where the corresponding (p_i, q_i) are known (oriented points). The *Picard-Lindelöf* Theorem [29] guarantees the existence and uniqueness of these *characteristic strips*. However, there are no guarantees that the surface is uniquely recovered from these strips. The next section shows that if the initial conditions $(u_i, v_i, \tilde{x}_i, p_i, q_i)$ of the *characteristic system* belong to a curve, the *initial curve*, that fulfills some constraints, the *characteristic strips* define a unique surface.

4.3 Existence and Uniqueness of Local Solutions

Monge's theory provides us with a way to reconstruct the surface solution \mathcal{S}_s via characteristic strips. This requires one to define a strip:

$$c_0(s) = (u_0(s), v_0(s), x_0(s), p_0(s), q_0(s)) \in \mathbb{R}^5, \quad (19)$$

called the *initial strip*. The first three dimensions of $c_0(s)$ represent the *initial curve* denoted by $\gamma_0(s) = (u_0(s), v_0(s), x_0(s))$. In Monge's theory, the initial strip has to comply with the following conditions:

- Compatibility condition 1:

$$\begin{cases} \frac{dx_0}{ds} = \frac{du_0}{ds}p_0 + \frac{dv_0}{ds}q_0 \\ F(u_0(s), v_0(s), x_0(s), p_0(s), q_0(s)) = 0 \end{cases} \quad (20)$$

- Compatibility condition 2:

$$\left| \left(\begin{array}{cc} \frac{du_0}{ds} & \frac{dv_0}{ds} \\ F_p(\gamma_0(s), p_0(s), q_0(s)) & F_q(\gamma_0(s), p_0(s), q_0(s)) \end{array} \right) \right| \neq 0. \quad (21)$$

Both conditions have a geometric interpretation. Compatibility condition 1 means that the velocity vector of the initial curve belongs to the tangent plane of the solution surface and that the initial condition must fulfill the PDE (14). Compatibility condition 2 tells us that an initial strip cannot be a solution of the characteristic system (16). Failure to comply with this would mean that for each point of the initial strip, solving the characteristic system (16), one recovers the initial strip itself. This means that one cannot recover the solution surface in Ω around the initial strip.

Observe that two *initial curves* that fulfill the compatibility conditions and intersect at a point p , determine the same *characteristic strip*. In other words they are intrinsic to the surface. We can also use intersection of curves to compute characteristic strips.

Given conditions (20) and (21), the following Theorem ensures the existence of a local solution around

the initial strip. The proof can be found in [25] and is a central result of Monge's theory. It relies on the *inverse function* and *Picard-Lindelöf* Theorems.

Theorem 2 (Monge) *Let $F(u, v, x, p, q) = 0$ be a first-order PDE where $\Omega \subset \mathbb{R}^3 \times \mathbb{R}^2$, $F : \Omega \mapsto \mathbb{R}$ and $F \in \mathcal{C}^2(\Omega)$ with $|F_p| + |F_q| > 0$. Let $\gamma_0(s) = (u_0(s), v_0(s), x_0(s))$ be an initial curve with continuous second-order derivatives and let $p_0(s)$ and $q_0(s)$ be functions with continuous first-order derivatives that satisfy the compatibility conditions (20) and (21). Then there exists a neighbourhood $G \subset \mathbb{R}^2$ of $(u_0(s), v_0(s))$ and a unique function $\phi : G \subset \mathbb{R}^2 \mapsto \mathbb{R}$ that satisfies:*

$$\begin{cases} \phi(u_0(s), v_0(s)) = x_0(s) \\ \phi_u(u_0(s), v_0(s)) = p_0(s) \\ \phi_v(u_0(s), v_0(s)) = q_0(s) \\ F(u, v, \phi(u, v), \phi_u(u, v), \phi_v(u, v)) = 0 \end{cases} \quad \begin{matrix} s \in I \\ (u, v) \in G \end{matrix} \quad (22)$$

Theorem 2 states that given an initial strip $r_0(s) = (u_0(s), v_0(s), x_0(s), p_0(s), q_0(s))$ that meets the compatibility conditions of equations (20) and (21), we can guarantee the solution of the PDE to be unique in a neighbourhood $G \subset \mathbb{R}^2$ of $(u_0(s), v_0(s))$. This can be accomplished by solving the characteristic system using the initial strip as initialization. This gives the surface $(u(s, t), v(s, t), x(s, t), p(s, t), q(s, t))$. We then search for the mapping $\varphi : (u, v) \rightarrow (s, t)$ to recover the surface solution $\phi(u, v) = x(\varphi(u, v))$.

In practice however, the boundary conditions will most likely be given as curves rather than strips. Because a curve $\gamma_0(s) = (u_0(s), v_0(s), x_0(s))$ is a weaker condition than a strip, we can expect a weaker result on solution uniqueness. We answer this equation precisely by giving the following theorem.

Theorem 3 *For an initial curve $\gamma_0(s) = (u_0(s), v_0(s), \tilde{x}_0(s))$ that complies with the compatibility conditions (20) and (21), the perspective reconstruction PDE (12) in the dependent variable \tilde{x} has a maximum of two local solutions $\tilde{x}_1(u, v)$ and $\tilde{x}_2(u, v)$.*

Proof By defining F from equation (12) and substituting into equation (20) we obtain a system composed of a linear and a quadratic equations in (p, q) . This system has a maximum of two solutions $(p_1(s), q_1(s))$ and $(p_2(s), q_2(s))$. Consequently, a maximum of two initial strips $(\gamma_0(s), p_1(s), q_1(s))$ and $(\gamma_0(s), p_2(s), q_2(s))$ exist with the same initial curve $\gamma_0(s)$. Using Theorem 2, we conclude that there exist a maximum of two local solutions $\tilde{x}_1(u, v)$ and $\tilde{x}_2(u, v)$ with the same initial curve but a different initial strip. \square

4.4 Local Domains of Reconstruction

According to Theorem 2 and assuming that an initial strip is given, the solution of the PDE (14) is only guaranteed to exist and to be unique in an open domain near the initial strip denoted by the local domain G (a subset of the image plane) where we have $|F_p| + |F_q| > 0$ for any surface solution. Applying this result to the PDE (12) we show that the image domain can be partitioned into a set of local domains that limit the maximum number of solutions for the PDE (12). We first define the set \mathcal{H} of *critical points*, which are points in Ω where $|F_p| + |F_q| = 0$.

Definition 2 A point $P_i \in \Omega$ is a critical point of a solution surface \mathcal{S}_s if $F_p(P_i) = 0$ and $F_q(P_i) = 0$. The set \mathcal{H} contains the critical points of \mathcal{S}_s in Ω :

$$\mathcal{H} = \{P_i \in \Omega | F_p = F_q = 0, F(P_i) = 0\} \quad (23)$$

Our next theorem shows that the critical points correspond to points in Ω where $p = q = 0$. Hence, they are points on the surface \mathcal{S} whose normal vector is parallel to the optical ray.

Theorem 4 Given a critical point $(u_i, v_i, x_i, p_i, q_i) \in \mathcal{H}$, the normal vector to the surface \mathcal{S} at the critical point is parallel to the optical ray $(u_i, v_i, 1)$.

Proof Using the equiareal reconstruction equation (10) we obtain F_p and F_q as:

$$\begin{cases} F_p = \frac{1}{\varepsilon^4} \left(\frac{(1+u^2)}{2} p + \frac{uv}{2} q \right) \\ F_q = \frac{1}{\varepsilon^4} \left(\frac{(1+v^2)}{2} q + \frac{uv}{2} p \right) \end{cases} \quad (24)$$

Rearranging equation (24) we have that F_p and F_q are obtained with the following linear system in p and q :

$$\begin{pmatrix} F_p \\ F_q \end{pmatrix} = \frac{1}{2\varepsilon^4} \begin{pmatrix} 1+u^2 & uv \\ uv & 1+v^2 \end{pmatrix} \begin{pmatrix} p \\ q \end{pmatrix} \quad (25)$$

This system is non-singular because the determinant of the system's matrix is $u^2 + v^2 + 1 > 0$. Therefore, $F_p = F_q = 0$ if and only if $p = q = 0$.

Using the depth-based embedding (\mathcal{I}, X_i) of equation (4), the normal vector field N is defined as:

$$N = X_u \times X_v = \left(\frac{\tilde{\rho}^2 u - \tilde{\rho} \tilde{\rho}_u \varepsilon^2}{\varepsilon^4}, \frac{\tilde{\rho}^2 v - \tilde{\rho} \tilde{\rho}_v \varepsilon^2}{\varepsilon^4}, \frac{\tilde{\rho}^2 + \tilde{\rho} \varepsilon^2 (\tilde{\rho}_u u + \tilde{\rho}_v v)}{\varepsilon^4} \right). \quad (26)$$

As $F_p = F_q = 0 \iff p = \tilde{x}_u = q = \tilde{x}_v = 0$, by using equation (11) we deduce that $\tilde{\rho}_u = 0$ and $\tilde{\rho}_v = 0$. Consequently, substituting into equation (26) we obtain:

$$N = \frac{\tilde{\rho}^2}{\varepsilon^4} (u, v, 1), \quad (27)$$

which is colinear with the optical ray $(u, v, 1)$. \square

Using Theorem 4 we classify the critical points into three categories: 1) isolated critical points, 2) critical curves and 3) critical surfaces. For instance if \mathcal{S} is a plane, \mathcal{H} contains a single isolated critical point and if \mathcal{S} is the visible portion of the sphere centered at the camera center, \mathcal{H} contains all points in \mathcal{S} and all critical points form a critical surface. We give a formal characterization of the different categories of critical points in appendix A.

The projection of the set \mathcal{H} in the image plane is denoted by \mathcal{H}_i . It splits the image domain into subdomains where the reconstruction solution is unique thanks to Theorem 2 for a given initial strip. The set \mathcal{H}_i can be found by solving the characteristic system (16) for each initial condition and searching along the characteristic strips the points where $p = q = 0$. This strategy is not practically relevant because the numerical ODE solvers that can be used to solve the characteristic system are unstable around critical points. We now show that \mathcal{H}_i can be found without solving the characteristic system. This allows one to find an upper bound on the number of global solutions to the PDE (12) given an initial strip.

Setting $\tilde{\rho}_u = \tilde{\rho}_v = 0$ (a consequence of $p = q = 0$) in equation (10) we obtain the following surface, defined by the function $\tilde{x}_{max} : \mathbb{R}^2 \mapsto \mathbb{R}$:

$$\tilde{x}_{max} = |\varepsilon^3| \sqrt{\bar{U}}. \quad (28)$$

that we call the *maximal surface* and denote by \mathcal{S}_C . The maximal surface is not a solution of the reconstruction PDE (12) but it is tangent to any possible solution at the critical points. We define \mathcal{H}_C as the set of all critical points contained by all the solutions of the reconstruction PDE (12). Therefore, \mathcal{H}_C contains \mathcal{H} . The next theorem proves that the extrema of the *maximal surface* forms the set \mathcal{H}_C .

Theorem 5 The set of all critical points for all the solutions \mathcal{H}_C is the set of all extrema of the maximal surface \mathcal{S}_C .

Proof The maximal surface \mathcal{S}_C is parametrized as:

$$X_{max}(u, v) = (u, v, \tilde{x}_{max}), \quad (29)$$

where \tilde{x}_{max} is given by equation (28). By definition \mathcal{S}_C only fulfills the PDE (12) at the extrema of \tilde{x}_{max} where $\frac{\partial \tilde{x}_{max}}{\partial u} = \frac{\partial \tilde{x}_{max}}{\partial v} = 0$. Therefore, they are critical points and they are included in \mathcal{H}_C . Now, for any particular solution surface \mathcal{S}_s parametrized with (u, v, \tilde{x}) we have $p = q = 0$ at a critical point. By substitution in the PDE (12) we have that $\tilde{x} = \tilde{x}_{max}$ at the critical point. Therefore it belongs to the maximal surface and it is one of its extrema. \square

According to Theorem 5, we can find \mathcal{H}_C directly from \mathcal{S}_C obtained using equation (28). As $\mathcal{H} \subset \mathcal{H}_C$ we use \mathcal{H}_C as a way to simplify the detection of the critical points \mathcal{H} of \mathcal{S}_s .

4.5 Uniqueness of Global Solutions

Using Theorem 2 we can guarantee the solution of the PDE (12) to be unique in a local domain near the initial strip where $|F_p| + |F_q| > 0$. Local domains are delimited by critical curves including also boundaries of critical surfaces. The effect of isolated critical points can be neglected as they do not generate multiple solutions. As a consequence, if our initial strip passes through every region delimited by these curves, Theorem 2 then guarantees the uniqueness of the reconstruction. Otherwise there may exist multiple solutions.

We propose a theorem and a corollary to formalize these properties. Theorem 6 studies the case where there exists a single critical curve that divides the image into two regions and the initial curve belongs to one of the regions. We show in that case that there is a maximum of two solutions. In Corollary 1 we extend the result to a case with n regions and the initial curve crossing m of them.

Theorem 6 *Given a surface \mathcal{S} parametrized with (\mathcal{I}, X_p) , a critical curve $c(t)$ that splits \mathcal{I} into 2 regions and an initial strip $r(s)$ that does not intersect $c(t)$, then the number of solutions is upper bounded by 2.*

Proof Fig. 4 shows a graphical representation of the theorem. Let $c(t) = (u(t), v(t), x_0)$ be the critical curve where by definition $\tilde{x}(u(t), v(t)) = x_0$ is constant along the curve and thus $\tilde{x}_u(u(t), v(t)) = 0$ and $\tilde{x}_v(u(t), v(t)) = 0$. The critical curve has associated the strip $(u(t), v(t), x_0, 0, 0)$. Assume that at $t = t_0$ the direction of the critical curve is aligned with the v axis (which can be ensured by a local change of variable in the PDE). In that case we have that $\frac{\partial^n \tilde{x}}{\partial v^n}(u(t), v(t)) = 0$ for all n . By assuming that \tilde{x} is analytic in $c(t)$ (i.e. it admits a convergent Taylor series in a neighbourhood of $c(t)$), there exists a local 2D neighbourhood $\Delta \subset \mathcal{I}$ of $(u(t_0), v(t_0))$ where $\tilde{x}_v = 0$ (and all its derivatives). Therefore, restricted to Δ the original reconstruction PDE can be transformed into the following first-order ODE in the independent variable u :

$$\frac{\tilde{x}^2}{\varepsilon^6} + \frac{\tilde{x}_u^2}{4\varepsilon^4}(1 + u^2) - \bar{U}(u, v_0) = 0, \quad (30)$$

where u is the independent variable and $v_0 = v(t_0)$. Note that a solution to equation (30) corresponds to

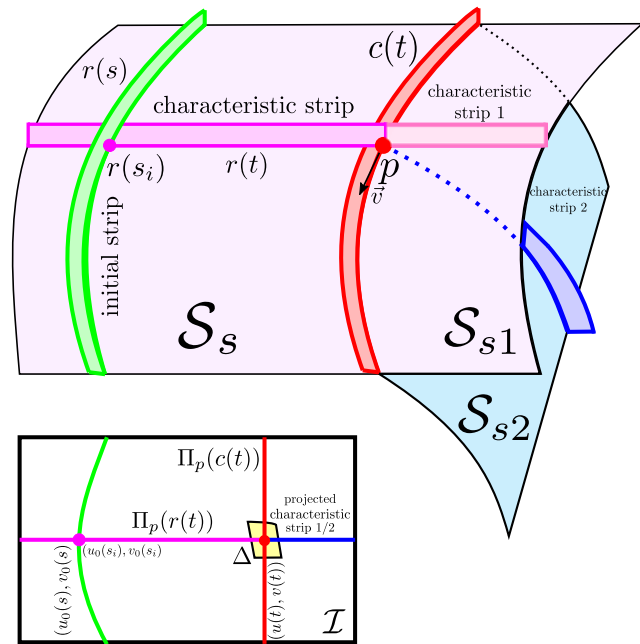


Fig. 4 Illustration of Theorem 6 where a critical curve $c(t)$ shown in red splits the domain into two regions. As the initial strip (green) does not intersect the critical curve $c(t)$, there exist two potential different solutions. The magenta characteristic strip $r(t)$ starts from the initial strip $r(s_i)$ and reaches the critical curve at point p . At this point two solutions of the strip are possible. The pink one lies on \mathcal{S}_{s1} , the blue one forms a second solution \mathcal{S}_{s2} .

the strip $(u, v_0, \tilde{x}, \tilde{x}_u, 0)$. We showed that the type of equation (30) has a maximum of two local solutions [11]. This implies that in Δ there exists a maximum of two strips for each point of the critical curve. By imposing integrability conditions to the bundle of strips derived from ODE (30) and the fact that there is a single critical curve in Δ , then there exists a maximum of two local solutions of the original PDE in Δ . By using Theorem 2 each solution in Δ , which contains points outside the critical curve, yields a single solution of the PDE in the corresponding region of \mathcal{I} split by $c(t)$. \square

Corollary 1 *Given a surface \mathcal{S} parametrized as (U, X_p) splitted in n regions by $n - 1$ critical curves and given an initial strip $r(s)$ that passes through m of these regions, the number of solutions is bounded by 2^{n-m} .*

Proof As the initial strip $r(s)$ passes through m regions, Theorem 2 guarantees the uniqueness of the solution in these m regions. We prove the bound by induction using the previous theorem applied for the $n - m$ regions. Let i be the induction variable. If $i = m + 1$ then the previous theorem guarantees that the number of solutions is bounded by 2. If $i = n - m$, by the induction hypothesis the number of solutions is bounded by 2^{n-m-1} .

When the characteristic curves reach the new critical curve, by Theorem 6 the number of possible solutions is bounded by 2. Consequently, the number of possible solutions for the iteration $i = n - m$ is bounded by $2 \cdot 2^{n-m-1} = 2^{n-m}$. \square

Note that given an initial curve $\gamma(s)$ that satisfies the compatibility conditions (20) and (21), there is a maximum of two local solutions upgrading the curve to form an initial strip, see Theorem 3. Applying Corollary 1 for each of the two strips upper bounds the number of solutions by 2^{n-m+1} .

Critical curves are unstable cases in equiareal SfT as any small perturbation in the camera location would remove them by decentering the spherical surface they belong to with respect to the coordinate origin. In addition we have observed in Sect. 5.1.2 that some of the ambiguities lead to unsmooth surfaces that even tend to invade the retinal plane at $z = 1$.

4.6 Reconstruction Algorithm

We propose a reconstruction algorithm to obtain the solutions of equiareal SfT based on our theoretical results. The inputs to our method are the template \mathcal{T} , an image \mathcal{I} of the deformed surface \mathcal{S} and an initial curve $\gamma(s)$ that lies on \mathcal{S} or a complete initial strip $c_0(s)$. The outputs are the surface \mathcal{S} or the multiple deformed surface solutions $\{\mathcal{S}_i\}$, the critical points and critical curves \mathcal{H} and the split regions. The algorithm has the following steps:

1. Compute the warp η from point correspondences between the image \mathcal{I} and the template’s texture map, defined in \mathcal{U} . Calculate the determinant of the first fundamental form $\bar{U}(u, v)$ from η and X_t .
2. Case 1: If an initial data curve $\gamma(s)$ is given, then, test if it satisfies the compatibility conditions (20) and (21). If only a finite number of points in the curve do not satisfy the conditions, split the curve and run the algorithm for each piece. Upgrade the initial curve to form the two initial strips $\phi(s)$ and $\psi(s)$ by solving the quadratic system (20) (Theorem 3 guarantees a maximum of two solutions). For each initial strip, we have at least one solution surface.
Case 2: If an initial strip $c_0(s)$ is given, then, test if the initial curve $\gamma(s)$ associated with $c_0(s)$ satisfies the compatibility conditions (20). Then, Theorem 2 guarantees a unique local solution around the initial strip.
3. Compute the *maximal surface* from equation (28) and compute the set of *critical points* \mathcal{H}_c . If there

is any critical curve, compute \mathcal{H}_i and the partition of the image plane.

4. For each point $p = \gamma(t_i), t_i \in I$, solve the ODE system (16) with a generic ODE solver (we use the *Runge-Kutta* method) using $(\gamma(t_i), \phi(t_i), \psi(t_i))$ as initial strip. This gives a characteristic strip which is on the solution surface.
5. At the points where the characteristic curves meet a critical curve, compute the two possible solutions and continue the reconstruction for each branch.
6. Integrate all characteristic curves that belong to the same solution in a single surface.
7. Refine each surface as described in Appendix B. This uses the *Levenberg-Marquardt* algorithm to minimize a maximum a posteriori (MAP) cost.

In practice, computing the warp in Step 1. requires methods such as [43, 49] that solve deformable registration in the presence of occlusions, self-occlusions and mismatches. Besides, in case of self-occlusions the warp becomes piece wise differentiable [18]. This splits the surface in regions where our reconstruction method can be applied. When multiple *initial curves* occur we first reconstruct surface patches by solving the characteristic system independently for each initial curve. Those surface patches which intersect and share their normal vector are considered part of the same surface, thus enforcing spatial consistency. We can check the equality between tangent planes in the intersection area because the *characteristic system* (18) gives us the normal vectors through variables p and q .

5 Experimental Results

We evaluate our reconstruction algorithm with synthetic and real data. We compare our reconstruction algorithm with five different non-isometric SfT methods (*Bartoli12c* [8], *Malti13* [2], *Malti15* [32], *Haouchine14* [21] and *Ozgur16* [39]) and one isometric SfT method (*Chhatkuli17* [12]). We use *EquiA-r* to denote our method described in Sect. 4.6 and *EquiA* to denote our method without the refinement step 7. We also include two alternatives to our method. We denote by *EquiA-rci* the refinement step 7 initialized with the maximal surface obtained analytically from \bar{U} using equation (28). We denote by *EquiA-rc* the same method without including points from the initial curve in the refinement cost (with $\nu = 0$ in equation (33)).

We measure the depth Mean Square Error (MSE) between each 3D reconstruction and the ground truth to evaluate the reconstruction accuracy.

5.1 Synthetic Data

5.1.1 Regular Cases

We generate 10 random pieces of bending paper using the tool provided in [41]. Each shape represents an isometric deformation ϕ_i , with $i = 1, \dots, 10$, of the plane. We then generate a planar equiareal map Δ between two planes. We use the family of planar equiareal mappings from [15] with $\delta(r) = r$ giving:

$$\begin{aligned} \Delta_{\delta(r)} : \quad \mathbb{R}^2 &\mapsto \mathbb{R}^2 \\ (r \cos(\theta), r \sin(\theta)) &\mapsto (r \cos(\theta + \delta(r)), r \sin(\theta + \delta(r))) \end{aligned} \quad (31)$$

By composing isometric embeddings with planar equiareal maps we obtain equiareal embeddings of the plane $\varphi_i = \phi_i \circ \Delta$, with $i = 1, \dots, 10$. Fig. 5 shows some examples of these 3D equiareal maps. The com-

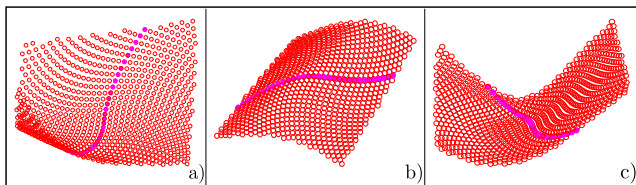


Fig. 5 Examples of synthesized equiareal embeddings resulting of an isometric embedding (a bent piece of paper) composed with a planar equiareal map. We show in magenta curves in the deformed surface that map to straight lines in the template.

plete setup is shown in Fig. 6.a.

We generate synthetic images of resolution 640×480 pixels using a camera with a focal length of 200 pixels. Each surface has a length comprised between 6cm and 10cm. None of the generated surfaces has critical curves. We use $N = 1000$ point correspondences between the template and each of the images. Gaussian noise is added to the images with $\sigma \in [0, 3]$ pixels. An initial strip is provided in order to run our algorithm *EquiA*, see Sect. 4.6. We perform 100 trials for each noise level. Fig. 6.b shows the average depth MSE of the 10 generated surfaces against noise level for *EquiA*. Standard deviation is also shown on the graph. We observe that the reconstruction degrades gracefully with the increase of noise.

In order to compare our method with other non-isometric methods, we repeat the same experiment with one surface and 10 trials for each noise value. This is because *Malti13* is very slow (several hours per noise value are required). Fig. 6.c shows the evaluation results. Our method obtain the best results for this experiment, nearly followed by *Ozgur16*. *Haouchime14* is

competitive but only in the absence of noise. *Malti15* is fast but much less accurate than the other methods. *Malti13* obtained the worst results. *Chhatkuli17* was not evaluated in this experiment as it consistently provides a very high error.

EquiA and *Ozgur16* show similar results in the previous experiment. There however exist cases where *Ozgur16* fails to recover the surface. We show such a case in Fig. 7 using synthetic data. We simulate the equiareal deformation of a cylindrical *template* with radius equal to 1. This surface is stretched along the x -axis. To preserve the area, the cylindrical surface is shrunk along the y -axis with a factor of 1.5. This way, the transformation is a 3D equiareal map. We observe that *Ozgur16* does not recover the correct shape even after more than 10,000 iterations, while *EquiA* accurately reconstructs the shape.

5.1.2 Degenerate Cases

Fig. 8.a shows two surfaces (magenta and green) that are equiareal deformations of the plane and have the same perspective projection. The magenta surface belongs to a cylinder with a symmetry axis on the xy -plane that passes through the camera center. This means that this cylinder has a critical curve (see remark 2 in appendix A). By computing \mathcal{H}_C we find this critical curve, that splits the image domain in two regions. In this example the initial curve is contained in one of the regions and according to Theorem 6 there is a maximum of two solutions to the same reconstruction PDE (12). Solving the PDE (12) we find two solutions depicted in Fig. 8.a as the green and magenta surfaces. The green surface is equal to the cylinder in the region that contains the initial curve but it differs from the cylinder in the other region. Fig. 8.a shows the maximal surface in red. As mentioned in Sect. 4.5, these are degenerate cases of our method as a small perturbation in the camera position would remove the ambiguities. Fig. 8.b shows the results of *EquiA-rci*, initializing the method with the maximal surface (red) and adding anchor points from the solution closer to the camera (green). The reconstruction result after refinement is displayed in blue. Fig. 8.c shows the results of *EquiA-rc* by initializing the method with the maximal surface (red). The reconstruction result (blue) converges to the cylindrical solution (magenta), which is closer to the maximal surface. This experiment confirms that the refinement algorithm converges to a local minimum and that it is strongly influenced by the initialization.

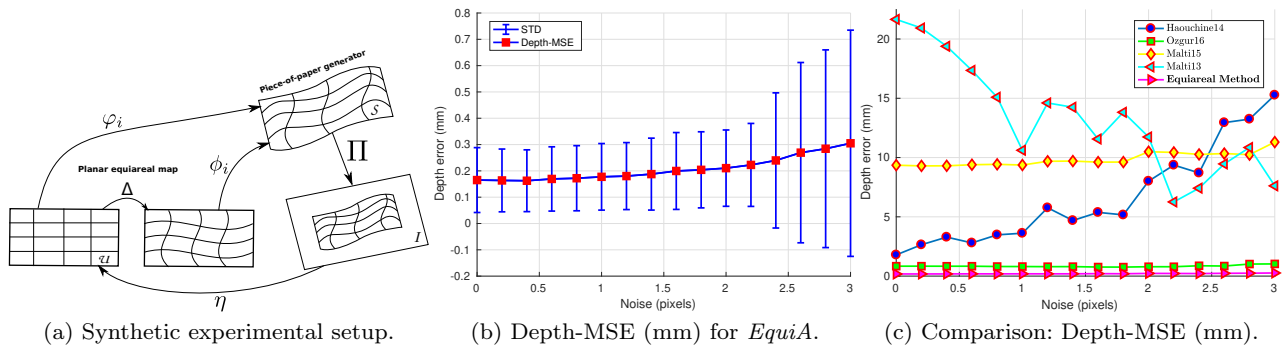


Fig. 6 Synthetic data experiments.

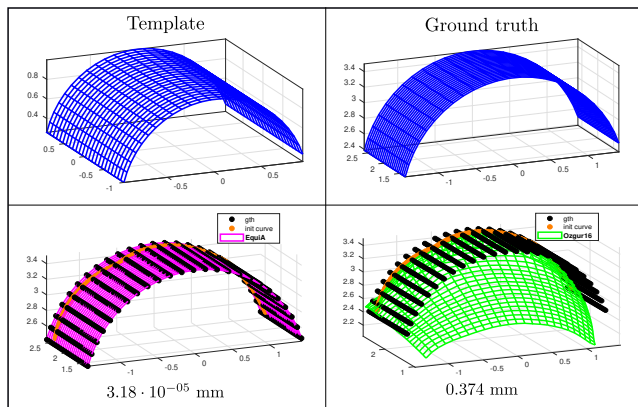


Fig. 7 The original cylindrical surface (*template*) is stretched by a factor 1.5 (*ground truth*). The result of *EquiA* is represented in magenta and *Ozгур16* in green. The initial curve is in orange. We show the depth error in both cases at the bottom.

5.1.3 Influence of the Initial Strip

We evaluate the influence of the *initial strip* (*initial curve*) in our reconstruction method (*EquiA* and *EquiA-r*), see Fig. 9. The experiment consists of the reconstruction of a cylindrical surface using different initial curves. The *initial curves* are represented with magenta and orange points in the first and second rows respectively. The first row in Fig. 9 shows the *characteristic curves* computed by *EquiA*. The second row shows the reconstruction after the refinement step *EquiA-r*. The first four columns (9.a-9.f, 9.b-9.g, 9.c-9.h, 9.d-9.i) represent different rotations of the same *initial curve* with respect to the center of the surface. We rotate the curve by 20° on each step. We observe that the reconstructed curves derived from the *initial curve* follow the same direction in all cases. As was mentioned in Sect. 4.3, characteristic strips are intrinsic to the surface and do not depend on the shape of the *initial curve*. However the shape of the *initial curve* does affect the amount of reconstructed area, as is observed by comparing 9.a with 9.d. In fact, in the limit case where

the *initial curve* does not comply with the compatibility conditions, the reconstructed area is degenerate and becomes the *initial curve* itself. We also show that the entire domain can be completely recovered using our refinement method *EquiA-r* (second row of Fig. 9).

The last column of Fig. 9 represents the reconstruction of the cylindrical surface using a circumference as *initial curve*. The *characteristic curves* obtained by *EquiA* with this *initial condition* 9.e are exactly the same in all cases as we mentioned previously.

5.2 Real Data

5.2.1 Wide-Baseline Datasets

We propose experiments with 6 different datasets. *DS1*, *DS2* and *DS3* show the stretching of three different t-shirts, *DS4* shows large stretching of an elastic fabric, *DS5* shows the deformation of a balloon and finally, *DS6* shows the deformation of an elastic sock. We use Microsoft’s Kinect 2 to grab 1920×1080 pixels RGB images and 512×424 pixels depth images used for ground-truth. Kinect 2 has a maximum range of 4.5m and a 60 degrees field of view with millimeter accuracy. As we mention in Sect. 4.5, the existence of critical curves is possible (see the Sect. 5.1.2) but practically improbable. None of the recorded datasets contain critical curves. Therefore, the subset \mathcal{H} only contains a finite set of critical points and there will be a single solution. We use an *initial strip* in all real experiments except for *Equi-rc* which does not require it. In case of giving an *initial curve*, we use *EquiA-rc* method to disambiguate from both two solutions as it usually gives a solution closed to the true surface. In some practical cases, the *initial strip* can be obtained trough isometric SFT in areas where the objects were isometrically deformed, or from rigid areas using SfM.

We first compare *EquiA* against the isometric SFT method *Chhatkuli17*. We use a piece of bending paper with a strong isometric deformation. We provide

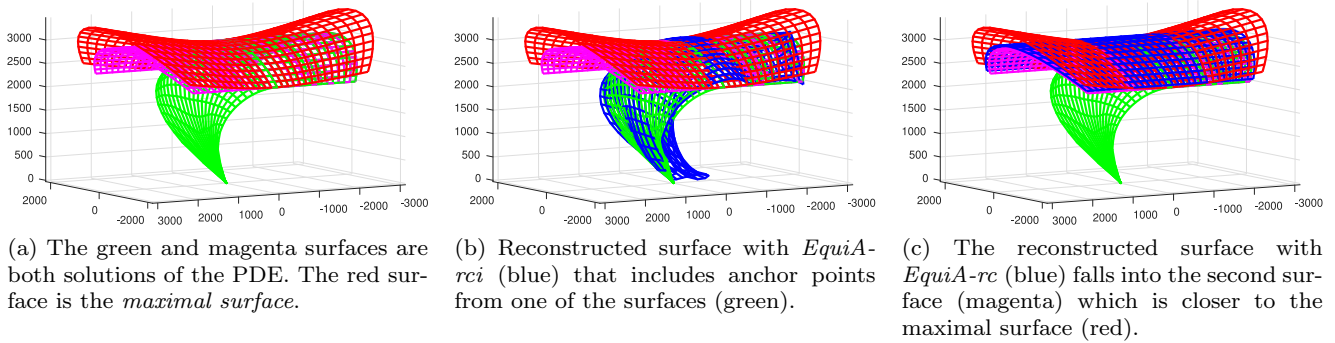


Fig. 8 Double solutions in the reconstruction of a cylinder with the perspective camera.

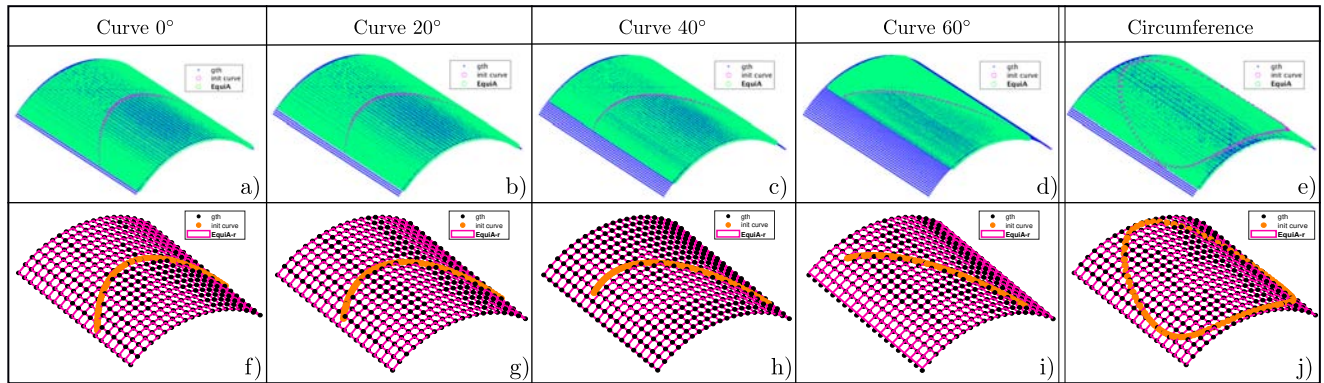


Fig. 9 Reconstruction of a cylinder with different *initial strips*. The first row shows the characteristic strips obtained with *EquiA*. The first four columns use the same initial curve rotated different angles. The fifth column uses a circumference as initial curve. The last row shows the result after using the refinement step *EquiA-r*. See Sect. 5.1.3 for more details.

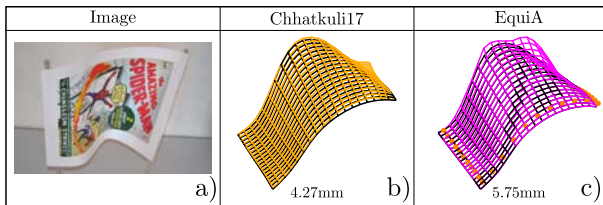


Fig. 10 Isometric deformation of a piece of paper. *Chhatkuli17* achieves excellent shape accuracy without any initial curve (orange points).

EquiA with an *initial strip* taken from the ground-truth shape. Fig. 10 shows the reconstruction results and the depth error of both methods in millimeters. As expected *Chhatkuli17* is very accurate in this case, not requiring the *initial curve*. *EquiA* obtains also very good results despite the fact that the equiareal model is much less constrained than isometry.

We now compare our equiareal SfT methods against the aforementioned state-of-the-art non-isometric SfT methods and *Chhatkuli2017* using six different datasets of common objects undergoing elastic deformations. An initial strip is provided for the equiareal algorithms *EquiA*, *EquiA-r*, *EquiA-rci* except for *EquiA-rc*. The

non-isometric SfT methods also use it as boundary conditions but not the isometric one. We show the results in Fig. 11. We provide for each experiment the coefficient of non-equiareality for all methods. This coefficient is a percentage computed by averaging the difference between the determinant of the first fundamental form before (template) and after the deformation:

$$\alpha_{\text{n-eq}} = \frac{100}{|N|} \sum_{p_i \in P} \frac{|\bar{U}(p_i) - U_i(p_i)|}{|\bar{U}(p_i)|} \quad (\%), \quad (32)$$

where $P \subset \mathcal{I}$ is a discrete set of N points.

As can be seen, the proposed equiareal methods obtain the best results for all the proposed experiments, particularly *EquiA-r*. *EquiA* obtains better results for *DS1*, *DS2*, *DS3* and *DS6* compared with the other methods, but *Haouchine14* achieves better results than *EquiA* in *DS4* and *DS5*. If we refine the solutions (*EquiA-r*), we obtain the best results in *DS1*, *DS2*, *DS3*, *DS5* and *DS6*. The refinement method *EquiA-rci* obtains better results than *Haouchine14* in all the experiments, shares the best result with *EquiA-r* in *DS2*, *DS5* and *DS6* and obtains the best result in *DS4*. The version without initial conditions *EquiA-rc* also has very good results and is better than the other methods in


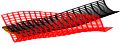
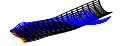

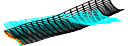
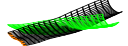

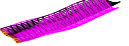





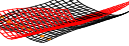
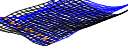
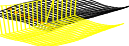
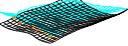
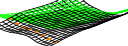

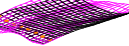

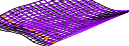
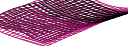


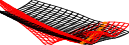
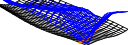

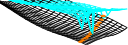
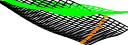

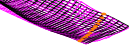

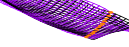
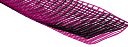
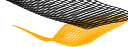


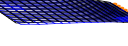











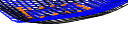











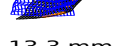
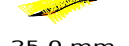








DS1 α_{n-eq} 13.67%		Bartoli12  24.7 mm	Haouchine14  13.2 mm	Malti15  59.1 mm	Matli13  15.5 mm	Ozgur16  16.9 mm
DS1 α_{n-eq} 13.67%		EquiA  7.8 mm	EquiA-r  4.9 mm	EquiA-rci  6.1 mm	EquiA-rc  10.1 mm	Chhatkuli17  51.0 mm
DS2 α_{n-eq} 17.55%		Bartoli12  17.3 mm	Haouchine14  8.9 mm	Malti15  49.9 mm	Matli13  14.2 mm	Ozgur16  12.8 mm
DS2 α_{n-eq} 17.55%		EquiA  8.5 mm	EquiA-r  2.7 mm	EquiA-rci  2.7 mm	EquiA-rc  6.3 mm	Chhatkuli17  70.6 mm
DS3 α_{n-eq} 15.67%		Bartoli12  32.0 mm	Haouchine14  23.9 mm	Malti15  580.2 mm	Matli13  32.3 mm	Ozgur16  29.0 mm
DS3 α_{n-eq} 15.67%		EquiA  3.8 mm	EquiA-r  3.2 mm	EquiA-rci  3.3 mm	EquiA-rc  7.0 mm	Chhatkuli17  74.9 mm
DS4 α_{n-eq} 20.41%		Bartoli12  332.7 mm	Haouchine14  45.3 mm	Malti15  90.1 mm	Matli13  48.8 mm	Ozgur16  135.2 mm
DS4 α_{n-eq} 20.41%		EquiA  49.4 mm	EquiA-r  29.0 mm	EquiA-rci  28.3 mm	EquiA-rc  40.5 mm	Chhatkuli17  100.0 mm
DS5 α_{n-eq} 35.55%		Bartoli12  5.2 mm	Haouchine14  2.9 mm	Malti15  9.5 mm	Matli13  6.0 mm	Ozgur16  5.9 mm
DS5 α_{n-eq} 35.55%		EquiA  4.9 mm	EquiA-r  2.7 mm	EquiA-rci  2.7 mm	EquiA-rc  3.7 mm	Chhatkuli17  12.1 mm
DS6 α_{n-eq} 50.82%		Bartoli12  9.8 mm	Haouchine14  13.3 mm	Malti15  25.0 mm	Matli13  24.7 mm	Ozgur16  20.6 mm
DS6 α_{n-eq} 50.82%		EquiA  1.7 mm	EquiA-r  1.4 mm	EquiA-rci  1.4 mm	EquiA-rc  18.7 mm	Chhatkuli17  172.3 mm

Fig. 11 Comparison of non-isometric SFT methods over DS1, DS2, DS3, DS4, DS5, DS6. The initial strip is in orange.

DS1, *DS2*, *DS3* and *DS4*. *Bartoli12* does not achieve very good results even with a small stretching in *DS1*, *DS3*. Besides, it takes substantial time to compute the reconstruction. *Malti15* is the quickest method but it gives the worst reconstruction error in *DS1*, *DS2*, *DS3*, *DS5* and *DS6*. *Malti13* obtains good results but it takes a much longer time compared to the other methods. *Ozgur16* obtains results similar to *Malti13* except for *DS4* but runs faster than *Malti13*, *Bartoli12* and *Haouchine14*. *Chhatkuli17* does not obtain good results in the relatively simple deformations shown in *DS1*, *DS2* and *DS3* as the amount of stretching in these three cases is enough to break isometry. However, it achieves better results than *Malti15* in experiments *DS1* and *DS3*, also improving over *Bartoli12* and *Ozgur16* in *DS4*. We can see that all versions of our equiareal method improve the other methods.

Choosing the best proposed method depends on the nature of the reconstruction problem and the information available *a priori*. *EquiA* achieves very good results. It is an analytical algorithm based on standard ODE solvers (*Runge-Kutta* method) which is fast and recovers all existing solutions. *EquiA-r* uses non-linear refinement initialized by *EquiA* and gives the best results in almost all our experiments. Both *EquiA* and *EquiA-r* require points from the initial curve. *EquiA-rci* also requires points from the initial curve but refinement is initialized with the *maximal surface*. It achieves good results but in general is less accurate than *EquiA-r*. It is interesting to observe that *EquiA-rc*, which does not need any initial curve and is initialized with the maximal surface, obtains comparable results with the other equiareal methods and definitely better than the other non-isometric methods compared.

Table 1 presents quantitative measures of computation time over the datasets *DS4*, *DS5* and *DS6* using a grid of 400 points. The experiment shows the average computation time of each method, fixing a maximum of 500 iterations. *Malti13* has the longest time, which is constant on the experiments as the maximum number of iterations is always reached. *Bartoli12* and *Haouchine14* obtain similar results. They are faster than *Malti13* and the convergence time is more dependent on the experiment. *Malti15*, *Ozgur16* and *EquiA* have a similar computation time at around 1 second. This is several orders of magnitude faster than the other methods. *EquiA-r*, *EquiA-rci*, *EquiA-rc* and *Chhatkuli17* have similar computation times in the order of several seconds. These measurements were made on a mid-range laptop computer (*Intel(R) Core(TM) i7-6700HQ CPU @ 2.60GHz*).

5.3 Video Datasets

We check the behaviour of our methods on video sequences. In this setup the 3D shape in the first frame is known and used as the initial condition for *EquiA-rc*. We compare this method with *Chhatkuli17* and the best elastic method, *Haouchine14*. Figs. 12 and 13 show two video sequences that correspond to frames of the datasets *DS1* and *DS4*. We evaluate the algorithms with several levels of frame dropping in the sequence (5 and 20 frames). Video sequences with a frame dropping of 20 show stronger deformations between consecutive frames than if we reconstruct the surfaces frame by frame. The refinement algorithm requires more iterations to converge to a local minimum.

Our algorithm obtains the best reconstruction in both experiments. It obtains a similar depth error for sequences with 1, 5 and 20 frame droppings. The algorithm converges quickly to the minimum. We observe this behaviour with *Chhatkuli17* but with a higher error due to the non-isometric deformations. *Haouchine14* outperforms *Chhatkuli17* but degrades with larger frame droppings. Besides, the number of iterations and the computation time is several orders of magnitude higher than our method's, see Table. 1.

6 Conclusions

We have given a theoretical framework based on Monge's theory to study the existence and uniqueness of SFT for equiareal deformations. This is the first paper that studies the ambiguities in SFT for non-isometric deformations. We have given the proof of existence of a maximum of two local solutions around an initial curve. We have proposed an analytical reconstruction algorithm based on standard numerical solvers for ODEs that obtains characteristic curves that are guaranteed to belong to the surface in a local domain. We have also showed how to identify the domain where the solution is unique and how to find the partitions of the image domain where Monge's existence theorem can be applied. We have showed empirical evidence that the method based on our theory is able to give accurate and stable reconstructions of real objects undergoing non-isometric deformations.

A Appendix: Classification of Critical Points

A.1 Isolated Critical Points

We define isolated critical points as follows.

	Bartoli12	Haouchine14	Malti15	Malti13	Ozgun16	EquiA	EquiA-r	EquiA-rci	EquiA-rc	Chhatkuli17
Mean-time (s)	301.92	334.53	1.25	981.77	0.97	1.40	3.55	3.14	14.48	6.90

Table 1 Mean computational time over datasets DS_4 , DS_5 and DS_5 . The experiment was made while fixing a maximum of 500 iterations per algorithm and using a grid of 400 points.

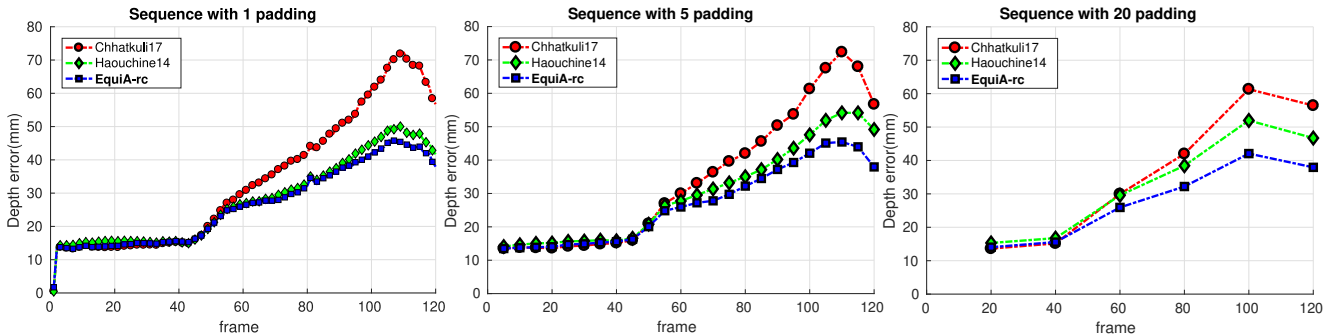


Fig. 12 Depth error in sequences with 1, 5 and 20 padding in the reconstruction of the dataset DS1.

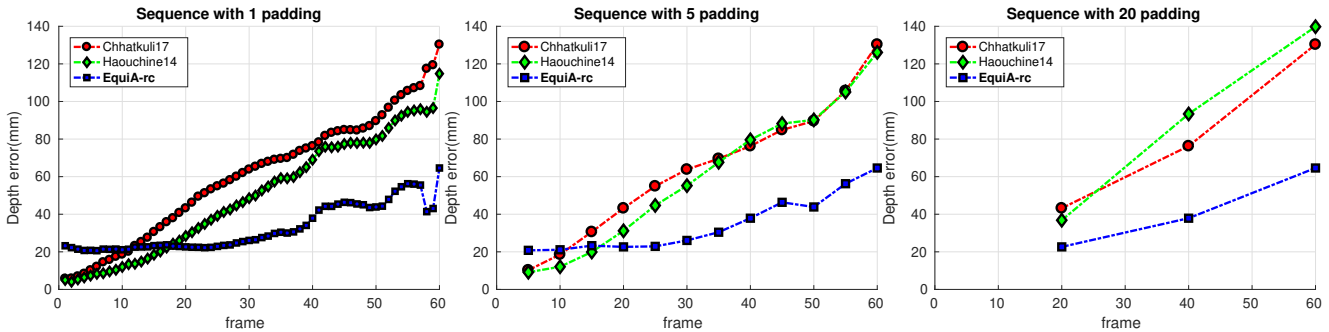


Fig. 13 Depth error in sequences with 1, 5 and 20 padding in the reconstruction of the dataset DS4.

Definition 3 A point p is an isolated critical point if it is a critical point ($\tilde{\rho}_u = \tilde{\rho}_v = 0$) and the Hessian of the depth function $\tilde{\rho}$ is non-degenerate.

Consequently, there must exist a neighbourhood around the critical point p where all points are non-critical except for the point p . By imposing integrability conditions, if the surface has a finite number of these points, there exists only one possible solution to the reconstruction PDE in the neighbourhood of p .

A.2 Critical Curves

Perspective critical curves are spherical curves. We prove that perspective critical curves are contained in a spherical surface whose center is located at the camera center. First of all, we define critical curves as follows.

Definition 4 A curve \mathcal{C} in the surface \mathcal{S} is a critical curve of the surface \mathcal{S} with respect to the perspective parametrization (\mathcal{I}, X_p) if all its points are critical ($\tilde{\rho}_u = \tilde{\rho}_v = 0$).

Theorem 7 If \mathcal{C} is a critical curve of a surface \mathcal{S} with respect to a perspective parametrization (U, X_p) , then, the curve \mathcal{C} belongs to a spherical surface whose center is located at the camera center.

Proof Fig. 14 illustrates the proof. Suppose that there exist a point p of the critical curve \mathcal{C} that does not belong to the

sphere \mathcal{S} whose center is placed at the camera center and has a radius of ρ_0 . There are two possibilities. If we assume that p is not a critical point, then, the curve is non-critical, contradicting the hypothesis. If we assume that p is a critical point, there is a neighbourhood $\Omega \subset \mathcal{C}$ of p where there exist a point $q \in \Omega$ that is a non-critical point, contradicting the hypothesis. So, critical curves are spherical curves that belong to a sphere whose radius is located on the camera coordinate center. \square

Remark 1 The only possible critical surfaces are the family of conformal spheres centred at the camera center.

Remark 2 Given any surface of revolution whose axis of symmetry is in the xy -plane, that contains the camera center. If its generatrix has a maximum, minimum or a saddle point at $t = 0$, then, the surface has as a critical curve formed by rotating this point around the generatrix. An example is a cylinder whose generatrix passes through the camera center, see Fig. 8.

B Refinement Method

We propose a refinement method for equiareal SfT based on minimizing a MAP compound cost functional. We proceed by defining the parametrization of \mathcal{S} from the template domain (\mathcal{U}, φ) , where $\varphi \in \mathcal{C}^2(\mathcal{U}, \mathbb{R}^3)$. From the commutative diagram shown in Fig. 2 we have that $X_i = \varphi \circ \eta$, where we recall that η is a known function. Working with φ instead of X_i

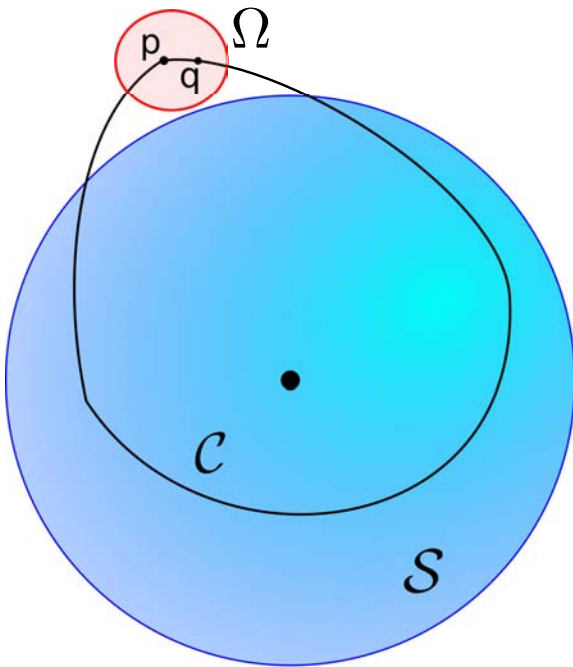


Fig. 14 Proof that critical curves are spherical curves that lie on a sphere whose center is located at the camera center. If the curve C is critical, then, if there is a point p out of the sphere S , either p is a critical point or there is a critical point q in its neighbourhood.

allows us to propose a MAP data cost. We define the set of correspondences between the template and the image as pairs of 2D points ($p^i \in \mathcal{U}, q^i \in \mathcal{I}$) for $i = 1, \dots, N$. Our cost functional is defined as:

$$\varepsilon[\varphi] = \lambda \varepsilon_{data}[\varphi] + \mu \varepsilon_{equiA}[\varphi] + \kappa \varepsilon_{smth}[\varphi] + \nu \varepsilon_{init}[\varphi], \quad (33)$$

where ε_{data} is the data term:

$$\varepsilon_{data}[\varphi] = \sum_{i=1}^N \|\Pi_p(\varphi(p^i)) - q^i\|^2. \quad (34)$$

ε_{equiA} is the equiareal constraint defined as:

$$\varepsilon_{equiA}[\varphi] = \sum_{p \in P} \|\mathbb{I}[\Delta(p)] - \mathbb{I}[\varphi(p)]\|^2, \quad (35)$$

where $P \subset \mathcal{U}$ is a regular grid of points defined in the template domain. $\mathbb{I}[X_t(p)]$ and $\mathbb{I}[\varphi(p)]$ are the determinants of the first fundamental form of surfaces X_t and φ respectively, evaluated at point p . ε_{smth} is a functional that minimizes the *bending energy* of the surface which encourages the solution to be smooth. Finally, the error of the initial conditions is defined by:

$$\varepsilon_{init}[\varphi] = \sum_{i \in I} \|\varphi(r^i) - s^i\|^2, \quad (36)$$

where I are the index set and r^i are points in \mathcal{U} that correspond to the set of 3D points $s^i \in S$ taken from the initial conditions. The set of hyperparameters λ , μ , κ and ν are scalars that control the importance of each functional and are fixed.

We use a B-spline to approximate φ which converts the variational problem of equation (33) into a non-convex polynomial cost function. We use the *Levenberg-Marquardt* algorithm to iteratively minimize the cost given an initial estimate of φ .

References

1. A. Varol, M. Salzmann, E. Tola, and P. Fua.: Template-free monocular reconstruction of deformable surfaces. In: CVPR (2009)
2. A. Malti, R. Hartley, A. Bartoli, and J.-H. Kim.: Monocular template-based 3D reconstruction of extensible surfaces with local linear elasticity. In: CVPR (2013)
3. Agudo, A., Agapito, L., Calvo, B., Montiel, J.M.: Good vibrations: A modal analysis approach for sequential non-rigid structure from motion. In: Proceedings of the IEEE Conference on Computer Vision and Pattern Recognition, pp. 1558–1565 (2014)
4. Agudo, A., Montiel, J.M.M., Agapito, L., Calvo, B.: Modal space: A physics-based model for sequential estimation of time-varying shape from monocular video. *Journal of Mathematical Imaging and Vision* **57**(1), 75–98 (2017)
5. Agudo, A., Moreno-Noguer, F.: Simultaneous pose and non-rigid shape with particle dynamics. In: Proceedings of the IEEE Conference on Computer Vision and Pattern Recognition, pp. 2179–2187 (2015)
6. Agudo, A., Moreno-Noguer, F., Calvo, B., Montiel, J.M.M.: Sequential non-rigid structure from motion using physical priors. *IEEE transactions on pattern analysis and machine intelligence* **38**(5), 979–994 (2016)
7. Akhter, I., Sheikh, Y., Khan, S., Kanade, T.: Nonrigid structure from motion in trajectory space. In: Advances in neural information processing systems, pp. 41–48 (2009)
8. Bartoli, A., Gérard, Y., Chadebecq, F., Collins, T., Pizarro, D.: Shape-from-template. *IEEE transactions on pattern analysis and machine intelligence* **37**(10), 2099–2118 (2015)
9. Bregler, C., Hertzmann, A., Biermann, H.: Recovering non-rigid 3D shape from image streams. In: CVPR. IEEE (2000)
10. Brunet, F., Bartoli, A., Hartley, R.I.: Monocular template-based 3D surface reconstruction: Convex inextensible and nonconvex isometric methods. *Computer Vision and Image Understanding* **125**, 138–154 (2014)
11. Casillas-Perez, D., Pizarro, D.: Solutions of quadratic first-order odes applied to computer vision problems. arXiv (2017). URL <https://arxiv.org/abs/1710.04265>
12. Chhatkuli, A., Pizarro, D., Bartoli, A., Collins, T.: A stable analytical framework for isometric shape-from-template by surface integration. *IEEE transactions on pattern analysis and machine intelligence* **39**(5), 833–850 (2017)
13. Del Bue, A.: A factorization approach to structure from motion with shape priors. In: Computer Vision and Pattern Recognition, 2008. CVPR 2008. IEEE Conference on, pp. 1–8. IEEE (2008)
14. Evans, L.C.: Partial Differential Equations, *Graduate Studies in Mathematics*, vol. 19, 2nd edn. American Mathematical Society (1998)
15. Floater, M.S., Hormann, K.: Surface parameterization: a tutorial and survey. In: Advances in multiresolution for geometric modelling, pp. 157–186. Springer (2005). DOI 10.1007/3-540-26808-1_9

16. Gallardo, M., Collins, T., Bartoli, A.: Using shading and a 3d template to reconstruct complex surface deformations. In: BMVC (2016)
17. Garg, R., Roussos, A., Agapito, L.: Dense variational reconstruction of non-rigid surfaces from monocular video. In: The IEEE Conference on Computer Vision and Pattern Recognition (CVPR) (2013)
18. Gay-Bellile, V., Bartoli, A., Sayd, P.: Direct estimation of nonrigid registrations with image-based self-occlusion reasoning. *IEEE Transactions on Pattern Analysis and Machine Intelligence* **32**(1), 87–104 (2010). DOI 10.1109/TPAMI.2008.265
19. Gotardo, P.F., Martinez, A.M.: Kernel non-rigid structure from motion. In: Computer Vision (ICCV), 2011 IEEE International Conference on, pp. 802–809. IEEE (2011)
20. Haouchine, N., Cotin, S.: Template-based monocular 3D recovery of elastic shapes using lagrangian multipliers. In: CVPR. IEEE (2017). DOI 10.1109/cvpr.2017.381
21. Haouchine, N., Dequidt, J., Berger, M.O., Cotin, S.: Single view augmentation of 3D elastic objects. In: ISMAR, pp. 229–236. IEEE (2014)
22. Haouchine, N., Roy, F., Untereiner, L., Cotin, S.: Using contours as boundary conditions for elastic registration during minimally invasive hepatic surgery. In: Intelligent Robots and Systems (IROS), 2016 IEEE/RSJ International Conference on, pp. 495–500. IEEE (2016)
23. Hartley, R., Zisserman, A.: Multiple view geometry in computer vision. Cambridge university press (2003)
24. J. Taylor, A. D. Jepson, and K. N. Kutulakos.: Non-rigid structure from locally-rigid motion. In: CVPR (2010)
25. John, F.: Partial differential equations, volume 1 of Applied Mathematical Sciences. Springer-Verlag, New York, (1982)
26. Koo, B., Özgür, E., Le Roy, B., Buc, E., Bartoli, A.: Deformable registration of a preoperative 3d liver volume to a laparoscopy image using contour and shading cues. In: International Conference on Medical Image Computing and Computer-Assisted Intervention, pp. 326–334. Springer (2017)
27. L. Torresani, A. Hertzmann and C. Bregler.: Nonrigid structure-from-motion: Estimating shape and motion with hierarchical priors. *IEEE Transactions on Pattern Analysis and Machine Intelligence* **30**(5), 878–892 (2008)
28. Li, J., Hero, A.O.: A fast spectral method for active 3d shape reconstruction. *Journal of Mathematical Imaging and Vision* **20**(1), 73–87 (2004). DOI 10.1023/B:JMIV.0000011324.14508.fb. URL <https://doi.org/10.1023/B:JMIV.0000011324.14508.fb>
29. Lindelof, E.: Sur l'application de la méthode des approximations successives aux équations différentielles ordinaires du premier ordre. *Comptes rendus hebdomadaires des séances de l'Académie des sciences. Bachelier and Gauthier-Villars (Paris)* (1894). URL <http://gallica.bnf.fr/ark:/12148/bpt6k3074r/f454.item.zoom#>
30. Liu-Yin, Q., Yu, R., Fitzgibbon, A., Agapito, L., Russell, C.: Better together: Joint reasoning for non-rigid 3d reconstruction with specularities and shading
31. Maier-Hein, L., Groch, A., Bartoli, A., Bodenstedt, S., Boissonnat, G., Chang, P.L., Clancy, N., Elson, D.S., Haase, S., Heim, E., et al.: Comparative validation of single-shot optical techniques for laparoscopic 3-d surface reconstruction. *IEEE transactions on medical imaging* **33**(10), 1913–1930 (2014)
32. Malti, A., Bartoli, A., Hartley, R.: A linear least-squares solution to elastic shape-from-template. In: CVPR, pp. 1629–1637 (2015)
33. Malti, A., Herzet, C.: Elastic shape-from-template with spatially sparse deforming forces. In: CVPR. IEEE (2017). DOI 10.1109/cvpr.2017.23
34. Monge, G.: Application de l'analyse à la géométrie: à l'usage de l'Ecole imperiale polytechnique. Ve. Bernard (1809). URL <https://books.google.es/books?id=ZmUSAAAAIAAJ>
35. Montenegro, A.A., Velho, L., Carvalho, P.C.P., Sossai, J.: Reconstruction of 3d object meshes from silhouette images. *Journal of Mathematical Imaging and Vision* **29**(2), 119–130 (2007). DOI 10.1007/s10851-007-0040-7. URL <https://doi.org/10.1007/s10851-007-0040-7>
36. Moreno-Noguer, F., Salzmann, M., Lepetit, V., Fua, P.: Capturing 3d stretchable surfaces from single images in closed form. In: Computer Vision and Pattern Recognition, 2009. CVPR 2009. IEEE Conference on, pp. 1842–1849. IEEE (2009)
37. Ngo, D.T., Östlund, J., Fua, P.: Template-based monocular 3d shape recovery using laplacian meshes. *IEEE transactions on pattern analysis and machine intelligence* **38**(1), 172–187 (2016)
38. Olsen, S.I., Bartoli, A.: Implicit non-rigid structure-from-motion with priors. *Journal of Mathematical Imaging and Vision* **31**(2), 233–244 (2008)
39. Özgür, E., Bartoli, A.: Particle-sft: A provably-convergent, fast shape-from-template algorithm. *International Journal of Computer Vision* **123**(2), 184–205 (2017)
40. Parashar, S., Pizarro, D., Bartoli, A.: Isometric non-rigid shape-from-motion with riemannian geometry solved in linear time. *IEEE transactions on pattern analysis and machine intelligence* (2017)
41. Perriollat, M., Bartoli, A.: A computational model of bounded developable surfaces with application to image-based three-dimensional reconstruction. *Computer Animation and Virtual Worlds* **24**(5), 459–476 (2013). DOI 10.1002/cav.1478
42. Perriollat, M., Hartley, R., Bartoli, A.: Monocular template-based reconstruction of inextensible surfaces. *International journal of computer vision* **95**(2), 124–137 (2011)
43. Pizarro, D., Bartoli, A.: Feature-based deformable surface detection with self-occlusion reasoning. *International Journal of Computer Vision* **97**(1), 54–70 (2012)
44. Russell, C., Yu, R., Agapito, L.: Video pop-up: Monocular 3d reconstruction of dynamic scenes. In: Computer Vision–ECCV 2014, pp. 583–598. Springer (2014)
45. S. Vicente and L. Agapito.: Soft inextensibility constraints for template-free non-rigid reconstruction. In: ECCV (2012)
46. Salzmann, M., Fua, P.: Reconstructing sharply folding surfaces: A convex formulation. In: Computer Vision and Pattern Recognition, 2009. CVPR 2009. IEEE Conference on, pp. 1054–1061. IEEE (2009)
47. Salzmann, M., Fua, P.: Linear local models for monocular reconstruction of deformable surfaces. *IEEE Transactions on Pattern Analysis and Machine Intelligence* **33**(5), 931–944 (2011)
48. Salzmann, M., Moreno-Noguer, F., Lepetit, V., Fua, P.: Closed-form solution to non-rigid 3d surface registration. *Computer Vision–ECCV 2008* pp. 581–594 (2008)
49. Sundaram, N., Brox, T., Keutzer, K.: Dense point trajectories by gpu-accelerated large displacement optical flow. In: European conference on computer vision, pp. 438–451. Springer (2010)

-
50. Varol, A., Shaji, A., Salzmann, M., Fua, P.: Monocular 3d reconstruction of locally textured surfaces. *IEEE transactions on pattern analysis and machine intelligence* **34**(6), 1118–1130 (2012)
 51. Vicente, S., Agapito, L.: Balloon shapes: Reconstructing and deforming objects with volume from images. In: *3DTV-Conference, 2013 International Conference on*, pp. 223–230. IEEE (2013)
 52. Y. Dai, H. Li, and M. He.: A simple prior-free method for non-rigid structure-from-motion factorization. In: *CVPR* (2012)